Remove Watermark Now

Journal of Geophysical Research: Oceans

RESEARCH ARTICLE
10.1029/2018JC013886

Structure and Formation of Anticyclonic Eddies in the Iceland Basin

Jian Zhao[1], Amy Bower[1], Jiayan Yang[1], Xiaopei Lin[2], and Chun Zhou[2]

[1]Woods Hole Oceanographic Institution, Woods Hole, MA, USA, [2]Physical Oceanography Laboratory/CIMST, Ocean University of China and Qingdao National Laboratory for Marine Science and Technology, Qingdao, China

Key Points:
- The anticyclonic eddy in the Iceland Basin has warm and salty subsurface waters in its core and substantial barotropic velocity
- One branch of the North Atlantic Current in the central Iceland Basin is superimposed onto the eddy, leading to asymmetric velocity structure
- The energy conversions estimated from model results suggest that both barotropic and baroclinic instabilities are involved to support the eddy growth

Correspondence to:
J. Zhao and X. Lin,
jzhao@whoi.edu;
linxiaop@ouc.edu.cn

Citation:
Zhao, J., Bower, A., Yang, J., Lin, X., & Zhou, C. (2018). Structure and formation of anticyclonic eddies in the Iceland Basin. *Journal of Geophysical Research: Oceans*, *123*, 5341–5359. https://doi.org/10.1029/2018JC013886

Received 6 FEB 2018
Accepted 19 JUN 2018
Accepted article online 27 JUN 2018
Published online 8 AUG 2018

©2018. American Geophysical Union. All Rights Reserved.

Abstract The Iceland Basin has the most energetic eddy activities in the subpolar North Atlantic. This study documents the structure for an anticyclonic eddy in the Iceland Basin using high-resolution hydrographic and velocity observations. The eddy core waters have lens-like structure with warm and salty features in the upper 1,000 m. The eddy distorts the density surface by doming the upper isopycnals and deepening the ones near the permanent pycnocline. The eddy has a diameter of about 120 km with substantial barotropic component in the velocity profiles. One branch of the North Atlantic Current in the central Iceland Basin is superimposed onto the eddy, leading to asymmetric velocity structure. Satellite maps show that eddy first shows up over the western slope of the Hatton Bank and moves westward to the central Iceland Basin. The waters enclosed in the eddy core share the same properties with Subpolar Mode Waters. Similar anticyclonic eddies are also found in high-resolution numerical model simulations, which is used to explore eddy formation. The model results reveal that the potential vorticity gradient prior to the eddy event change signs in both horizontal and vertical directions. This potential vorticity gradient structure meets the necessary condition for the barotropic and baroclinic instabilities. Further calculation of the energy conversions suggests that eddies extract mean potential energy from the large-scale isopycnal slope and gain the mean kinetic energy in the upper ocean. Therefore, both barotropic and baroclinic instabilities are involved to support the eddy growth.

pdfelement

1. Introduction

The subpolar North Atlantic Ocean is a vital region for the global climate. The northward moving warm waters release heat to the atmosphere and ultimately transform into the deep and intermediate water masses that feed the deep limb of the Atlantic meridional overturning circulation. The resulting meridional heat flux is pivotal to maintain a relatively warm climate in northern Europe and modulating the Arctic sea ice extent (Vellinga & Woods, 2002; Zhang, 2015). The large-scale circulation in this region is a superposition of both the horizontal gyre circulation and the Atlantic meridional overturning circulation. The cyclonic circulation can be diagnosed from the spatial pattern of the Absolute Dynamic Topography (ADT). The strongest horizontal gradients in the ADT map are found mainly near the topographic slopes, indicating that most currents are closely constrained by bathymetry (Figure 1a). An important element of the basin-scale circulation is the North Atlantic Current (NAC), which flows eastward from the western basin at about 52°N and crosses the Mid-Atlantic Ridge in several bands (Bower & von Appen, 2008; Rhein et al., 2011; Roessler et al., 2015). East of the Mid-Atlantic Ridge, the NAC main stream heads northeastward into the Iceland Basin and the Rockall Trough (Houpert et al., 2018). Some flows farther north into the Nordic Seas, and the remaining moves around the Reykjanes Ridge and continues into the Irminger Sea as part of the gyre circulation (Daniault et al., 2016; García-Ibáñez et al., 2015; Lherminier et al., 2010; Sarafanov et al., 2012).

In addition to the large-scale circulation, the mesoscale variability in the subpolar North Atlantic has been widely documented in observational and modeling studies (e.g., Eden & Böning, 2002; Heywood et al., 1994; Luo et al., 2011; Volkov, 2005; White & Heywood, 1995). The eddy kinetic energy (EKE), which is normally used to represent the intensity of the eddy activity, can be estimated from satellite altimetry and drifter measurements. Through analyses of the surface EKE field over different periods, several studies have found that enhanced eddy activities are mainly located in a few "hot spots" that are closely tied to the strong topographically constrained currents (e.g., Brandt et al., 2004; Heywood et al., 1994; Reverdin et al., 2003; Volkov, 2005; White & Heywood, 1995). We update the mean EKE map using the satellite altimetry data between 1993 and 2015 (Figure 1b). Consistent with the studies listed above, the highest EKE is located near the

Remove Watermark Now

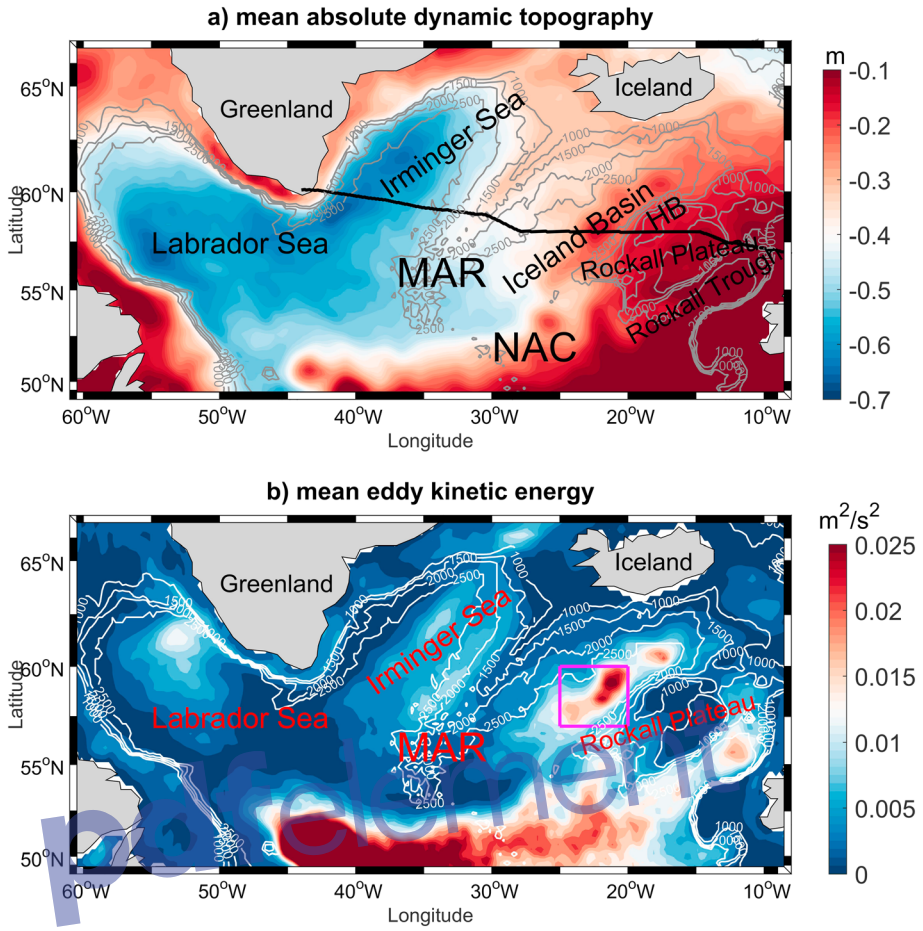

Figure 1. (a) Mean Absolute Dynamic Topography (ADT) computed from the satellite data between 1993 and 2015. The black line denotes the OSNAP East section. The acronyms are Mid-Atlantic-Ridge (MAR), Hatton Bank (HB), and North Atlantic Current (NAC). (b) Mean surface geostrophic eddy kinetic energy (EKE) calculated from the surface geostrophic velocity from the satellite data between 1993 and 2015. The magenta box represents the studied region in the Iceland Basin.

east and west flanks of the Rockall Plateau. The Irminger and Labrador Basins also have elevated EKE regions, typically associated with the boundary current over the topographic slopes. It should be mentioned that the satellite-derived EKE map shown here is in line with that estimated from drifter observations (Fratantoni, 2001; Jakobsen et al., 2003).

The most well-studied mesoscale eddy phenomenon in the subpolar North Atlantic is probably the formation of Irminger Rings (IRs) in the Labrador Sea. Their generation has been attributed to the instability of the boundary current in the eastern Labrador Sea (Bracco et al., 2008; Eden & Böning, 2002; Han & Ikeda, 1996; Heywood et al., 1994; White & Heywood, 1995; Wolfe & Cenedese, 2006). Carrying waters from the Irminger Current/West Greenland Current, the IRs can travel into the interior basin and significantly modify the hydrographic structure there and consequently affect the wintertime deep convection and restratification (DeJong et al., 2014; De Jong et al., 2016; Hátún et al., 2007; Lilly et al., 2003; Rykova et al., 2009). The fluxes associated with eddy propagation were found to significantly contribute to the heat and salt budgets in the interior Labrador Sea (Hátún et al., 2007; Lilly et al., 2003; Lilly & Rhines, 2002; Rykova et al., 2009).

While mesoscale eddies in the Irminger Sea were often noted in many observations (e.g., De Jong, 2010; De Jong et al., 2012; Holliday et al., 2009; Våge et al., 2011), their characteristics were examined more comprehensively by Fan et al. (2013). Using observations collected by the Central Irminger Sea mooring and a glider, they documented the eddy structure and examined their properties. These anticyclonic eddies were found to trap relatively warm and salty waters in their cores. Two eddy formation regions were

Remove Watermark Now

identified: the East Greenland Irminger Current near Cape Farewell and over the western flank of the Reykjanes Ridge.

Notable eddy activity in the Iceland Basin was recognized more than two decades ago. Synoptic cruise observations in the 1990s successfully captured individual cyclonic and anticyclonic eddies near 60°N in the Iceland Basin. For instance, a cyclonic eddy was detected in the vicinity of 61°N, 20°W during the UK's Biogeochemical Ocean Flux study in July 1991. The eddy had a size of 25 km in radius, and its geostrophic azimuthal current reached about 25 cm/s (Harris et al., 1997). The UK Plankton Reactivity in the Marine Environment (PRIME) program surveyed an anticyclonic eddy near 59°N, 20°W in summer 1996. The eddy was bottom reaching with a significant barotropic component. At 700 m depth the estimated radius was about 40 km with azimuthal speed of 40 cm/s (Martin et al., 1998; Wade & Heywood, 2001). Another anticyclonic eddy near 59.5°N, 21°W in June 1998 was found to carry similar characteristics as the PRIME eddy (Read & Pollard, 2001). Analyzing the Lagrangian trajectories of RAFOS floats deployed at middepth (σ_θ = 27.5), Shoosmith et al. (2005) concluded that comparable numbers of cyclonic and anticyclonic eddies exist in the Iceland Basin.

The above studies found that the physical motions associated with eddy have important impacts on the biogeochemical processes. The climatological near-surface satellite chlorophyll maps reveal that the central Iceland Basin has very limited biological production in July, perhaps due to nutrient limitation (Pacariz et al., 2016). However, the vertical motions near an anticyclonic eddy can transport nutrients into the surface-mixed layer and hence support production in local area (Woodward & Rees, 2001). More importantly, the recent North Atlantic Bloom Experiment further pointed out that the eddy-driven stratification and subduction in the Iceland Basin contribute to the initiation of the North Atlantic spring phytoplankton bloom and export of organic carbon into the deeper ocean (Mahadevan et al., 2012; Omand et al., 2015).

The above observations in the Iceland Basin mostly focused on the hydrographic features of the mesoscale eddy. Their velocity data were either limited to the upper ocean or inferred from hydrographic profiles with assumption of no motion at certain depth levels (e.g., Martin et al., 1998). It is well known that the currents in the Iceland basin have strong barotropic component (Van Aken, 1995), which is definitely not resolved by the thermal wind relation. In addition, none of these studies described the eddy generation process. In this study, we will make use of high-resolution hydrographic and velocity observations to document the structure for an anticyclonic eddy observed in the Iceland Basin in summer 2015. The source region and the mechanisms to support eddy development will be explored using outputs from a high-resolution numerical model.

pdfelement

2. Data and Methods

2.1. Observations

(a) Satellite altimetry

The ADT and surface geostrophic velocity fields between 1993 and 2015 were downloaded from the Copernicus Marine and Environment Monitoring Service (CMEMS) (http://www.marine.copernicus.eu). The EKE is defined as EKE = $[(u')^2 + (v')^2]/2$, where u' and v' were derived by removing the long-term mean from the total surface geostrophic velocity.

(b) Cruise data

As part of the Overturning in the subpolar North Atlantic Program (OSNAP; Lozier et al., 2017), hydrographic data were collected during a cruise in the Iceland Basin between June and July 2015. The conductivity/temperature/depth (CTD) profiles were acquired using a SeaBird SBE-911plus pumped system, and direct velocity profiles were measured using a dual-ADCP system (Lowered ADCP). The CTD data were calibrated using bottle samples collected during the cruise. The Lowered-ADCP data were processed using CTD profiles, absolute bottom-track velocity data, and upper-ocean shipboard ADCP velocity data to constrain the overall velocity profile (Thurnherr, 2011). The LADCP data were de-tided using the ADCP observations deployed in the Iceland Basin. The accuracy of Lowered-ADCP velocity profiles is estimated to be approximately 5 cm/s. In addition, we also analyze another trans-basin cruise performed in June 2014 by OSNAP, with an aim to display the large-scale hydrographic structure in the eastern subpolar ocean.

Remove Watermark Now

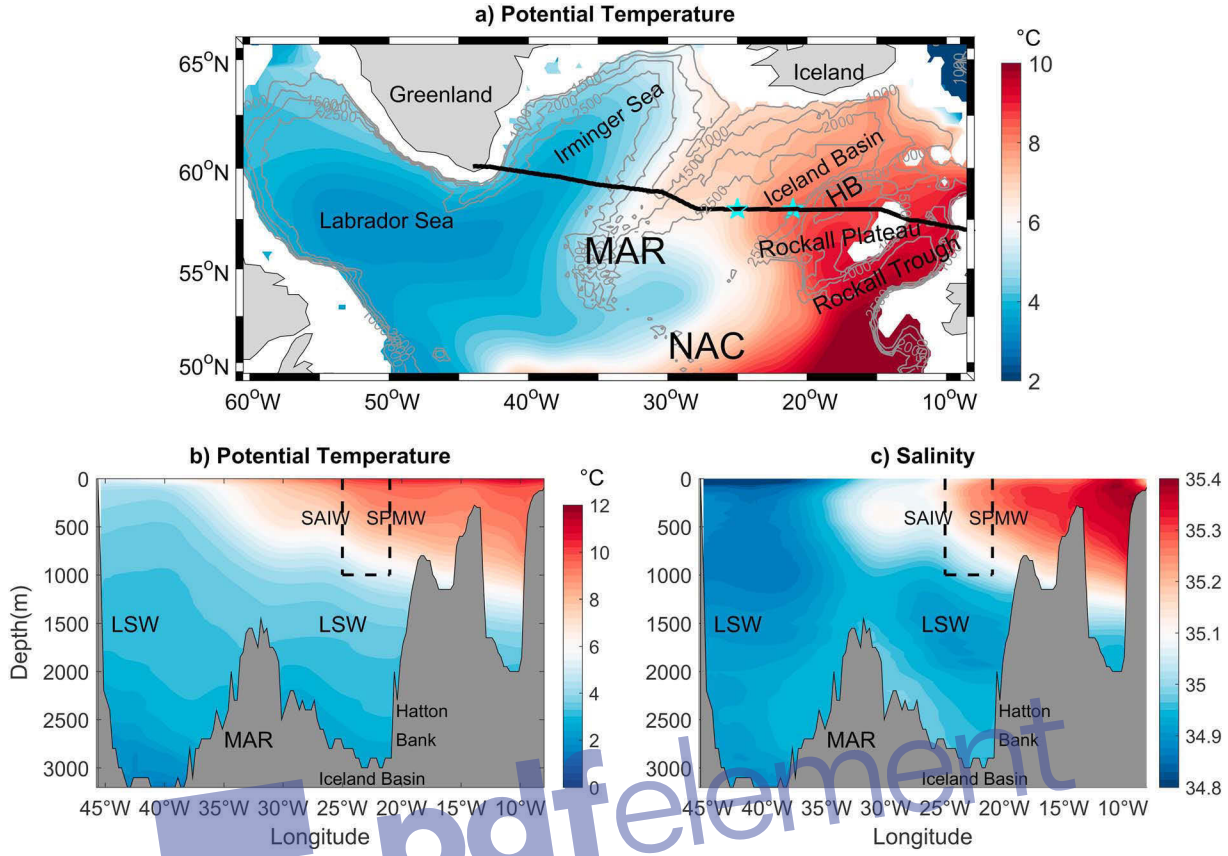

Figure 2. (a) Climatological potential temperature (unit: °C) at 500 m from the WOD2013 data. The black line denotes the OSNAP East. The light blue pentagons mark the endpoints for the glider section. (b) Mean potential temperature (unit:°C) and (c) salinity along the OSNAP East line from the WOD2013 data are shown, respectively. The black dashed boxes denote the region surveyed by glider. Water masses are marked: Subarctic Intermediate Water (SAIW), Subpolar Mode Waters (SPMW), and Labrador Sea Water (LSW). The Mid-Atlantic Ridge is labeled as MAR.

pdfelement

(c) Glider

A G2 Slocum glider was deployed in June 2015 as part of OSNAP to monitor the meridional volume and heat flux in the energetic Iceland Basin. The glider collected temperature, salinity, pressure, dissolved oxygen, optical backscatter, and fluorescence. The hydrographic data were measured by a Seabird pumped CTD package. The glider navigated in a sawtoothed pattern between the surface and about 1,000-m depth. The vehicle moved along 58°N with endpoints at 24.5°W and 21°W. Two OSNAP moorings M3 and M4 were deployed near the two endpoints. A one-way glider transect was usually completed in 7–10 days. The spacing between neighboring profiles had a mean distance of 3 km, but near the surface and 1,000 m turnaround points, distance ranged from hundreds of meters to 6 km. The CTD data were processed into profiles with vertical resolution of 1 m. In addition, the glider flight model, which incorporates the vehicle's underwater movement and surface positions, was used to estimate the depth-averaged velocity (i.e., over the top 1,000 m). The depth-averaged velocity consists of three major components: geostrophic, tidal, and wind-driven Ekman currents. The geostrophic component was taken as reference to estimate the velocity profiles. Please refer to Zhao et al. (2018) for more details. The data analyzed here were collected between June and November 2015.

2.2. High-Resolution Model Data

In addition to satellite and in situ observations, we use an eddy-resolving high-resolution (1/12°) HYbrid Coordinate Ocean Model (HYCOM) in this study. The model domain spans from 28°S to 80°N and has 32 layers in the vertical (Xu et al., 2010). The model performance was evaluated by Xu et al. (2012, 2013), who demonstrated that the simulated circulation in the subpolar North Atlantic agrees well with observations, particularly for the NAC and the boundary currents in the Labrador Sea. Our simulation was initialized by

Remove Watermark Now

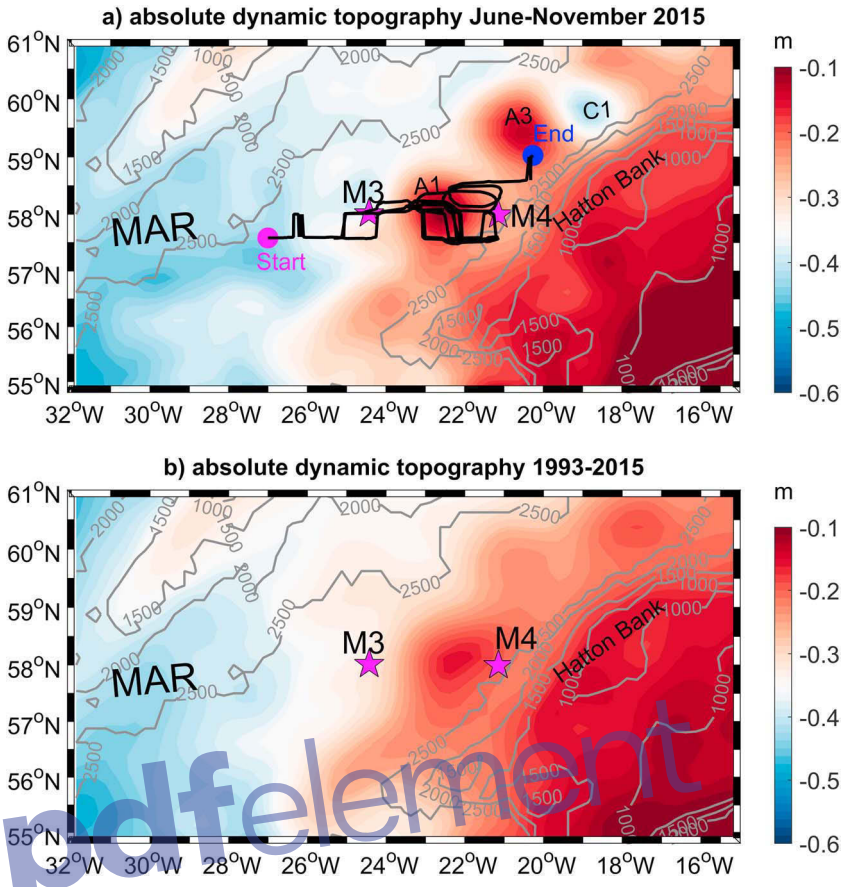

Figure 3. (a) Mean ADT during the eddy event (June–November 2015) is shown in color shading. Glider track is shown in black line. The magenta and blue dots denote the deployment and recovery places for the glider mission. The labels represent the OSNAP moorings M3 and M4, which are also the endpoints for the glider section. A1 and A3 are two anticyclones, and C1 is the cyclone in the Iceland Basin during this period. (b) Mean ADT from the satellite data between 1993 and 2015. This is the enlarge map of the magenta box in Figure 1b.

the spin up results from E026 in Xu et al. (2012). The model was further integrated for an additional 25 years, forced repeatedly by the daily National Centers for Environmental Prediction (NCEP) Climate Forecast System Reanalysis (CFSR) data set in year 1992. After that the model was integrated from 1992 to 2015 with daily forcing fields from NCEP CFSR data set. The model data used here are three-day outputs.

3. Eddy Characteristics in Observations

3.1. Water Masses in the Iceland Basin

To better understand the glider observations, we first present the large-scale hydrographic structure in the subpolar North Atlantic. The warm and salty subtropical-origin waters are transported into the eastern subpolar region and are further distributed by the cyclonic topography-following currents (Figure 2a). The relatively fresher and colder waters are located in the western subpolar region. As a result, the Subarctic Front (SAF) is set up by these large-scale water masses (Bersch, 2002). The SAF in the upper 1,000 m can be clearly identified from temperature and salinity sections along the OSNAP East line (Figures 2b and 2c). In the Iceland Basin, the SAF in the upper ocean separates the Subarctic Intermediate Water (SAIW) to the west from the SubPolar Mode Waters (SPMW). The SPMW is a broad water mass found throughout the subpolar region (Brambilla & Talley, 2008; McCartney & Talley, 1982; Pollard et al., 1996, 2004; Tsuchiya et al., 1992). The hydrographic properties of SPMW are modified by air-sea interactions, so that their specific temperature and salinity characteristics are regionally dependent. The SPMW in the Iceland Basin has thermohaline ranges of 6–9 °C and 35.10–35.25 (Stoll et al., 1996; Van Aken & Becker, 1996). The SAIW originates from the

pdfelement

Remove Watermark Now

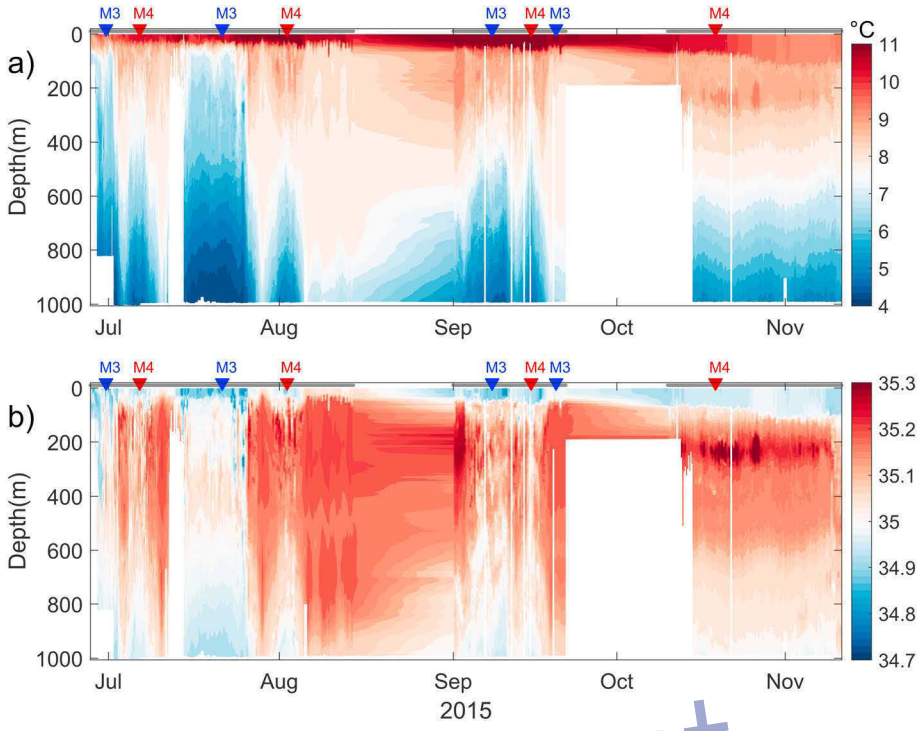

Figure 4. (a and b) Time series of temperature (unit: °C) and salinity sampled by the glider between June–November 2015 are displayed. The red and blue triangles represent the east (warm) and west (cold) endpoints of the sampling section. The grey lines near the sea surface indicate the periods when glider returned valid profiles.

pdfelement

western boundary of the subpolar gyre so that it is substantially fresher and colder (4–7 °C and 34.70–35.90; Arhan, 1990; Bersch, 2002; García-Ibáñez et al., 2015). According to thermal wind relation, the horizontal density gradient in the Iceland Basin corresponds to northward flow, which is the NAC branch in the Iceland Basin (Daniault et al., 2016; Pollard et al., 2004).

The section surveyed by glider is near the SAF in the Iceland Basin. When the glider was deployed in June 2015, there was an anticyclonic eddy (A1) between moorings M3 and M4 (Figure 3). Meanwhile, another anticyclonic eddy (A3) and a cyclonic eddy (C1) were located north of the glider section. This suggests that the Iceland Basin has rich eddy activities, which contribute to the elevated EKE shown in Figure 1b. When the glider was navigating along 58°N in 2015, the quasi-stationary anticyclonic eddy (A1) was well maintained and centered near the glider section. Therefore, the glider was able to sample the hydrographic structures within and surrounding the eddy. When the glider was recovered in November 2015, the eddy center had moved slightly northward to about 59°N.

The recorded temperature and salinity time series along the glider path indicate that the two end points for the glider transect were occupied by different water masses (Figure 4). The waters near M3 (western endpoint) are characterized by relatively cold and fresh SAIW ($\theta < 7$ °C, $S < 34.90$). M4 is embedded in the SPMW whose salinity is greater than 35.10 (Pollard et al., 2004).

3.2. Eddy Structure in Observations

Despite that the glider path was frequently detoured by the strong rotational currents associated with the anticyclonic eddy (A1), the vehicle did successfully cut across the eddy four times. A transect performed between 26 June and 10 July 2015 is selected as the representative section for the eddy (Figure 5a). During this period, the A1 eddy had a radius of about 60 km (1° in longitude). The satellite ADT map shows that a branch of northward current is located west of the eddy center. It exhibits a meridional coherent scale of more than 2° in latitude. This continuous current is associated with the NAC in the central Iceland Basin (Pollard et al., 2004). The hydrographic profiles collected by different glider dives between 25°W and 21°W were used to describe the vertical structure for the eddy (Figures 5b and 5c). The hydrographic properties

Remove Watermark Now

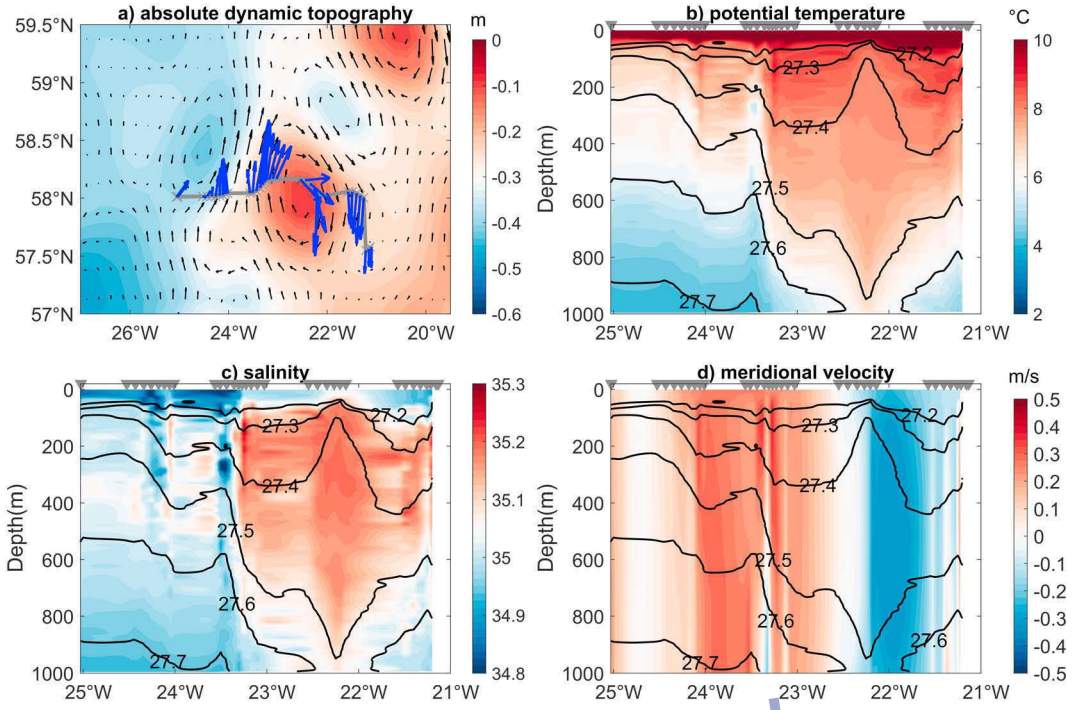

Figure 5. (a) The ADT map and the corresponding surface geostrophic velocity during a glider transect between 26 June and 10 July 2015. The depth-averaged currents in the upper 1,000 m derived from the glider flight model are displayed in blue vectors. The (b) potential temperature and (c) salinity are shown by color shadings. The potential density (σ_θ) is illustrated by black lines. (d) The meridional velocity estimated from the depth-averaged velocity and hydrographic profiles. The gray triangles near the surface mark the locations for each profile.

preprint

near the surface display uniform structures with temperature of 10–11°C and salinity of 34.80–34.95. This surface fresh layer is generally above the surface of σ_θ = 27.2 whose mean depth is about 50 m. Below σ_θ = 27.3, the isopycnals are obviously distorted. The isopycnal σ_θ = 27.4 is domed from 300 m near the eddy rim to about 100 m in the center. In contrast, σ_θ = 27.5 is depressed from about 400 m at the eddy edge to about 1,000 m in the eddy core. The majority of the subsurface waters in the eddy core are enclosed by the σ_θ surfaces of 27.4 and 27.5. They have potential temperature of 7.0–8.0 °C and salinity of 35.15–35.25. These homogeneous waters in the lens-like eddy core are distinct from the ambient waters. The subsurface waters west of the eddy are obviously colder and fresher, indicating that they are affected by the SAIW.

Ship-based CTD casts, taken between 19 and 28 June 2017, reveal the full water column structure of the A1 eddy. The casts were conducted along 58°N from 30°W to 19°W, so that it was wide enough to capture both the eddy and its surrounding area (Figure 6a). As shown by the satellite ADT map, there are rich mesoscale processes near the CTD section. These mesoscale phenomena apparently deviate the path of the northward flowing NAC. The most clearly seen continuous northward current occurs near 20°W, which is on the western slope of the Hatton Bank. The hydrographic structure measured by the CTD data is quite similar with the glider data, especially for the distorted isopycnals in the upper ocean as well as the warm and salty core waters. Overall, the eddy core is about 1,000 m thick and 120 km wide. The Labrador Sea Water (LSW) lies underneath σ_θ = 27.7, and its salinity range in the Iceland Basin is about 34.85–34.90 (Yashayaev, 2007). The Iceland-Scotland Overflow Water (ISOW), whose salinity is slightly higher than the LSW, occupies the bottom part of the water column.

The meridional velocity along 58°N was estimated from glider data and directly observed by the Lowered-ADCP. The observed subsurface velocity exhibits consistent structure with the surface geostrophic current in the satellite-derived ADT, which is a clockwise rotating current around the eddy between 25°W and 21°W. The overall pattern for the meridional velocity agrees well between the two methods (Figures 5d

Remove Watermark Now

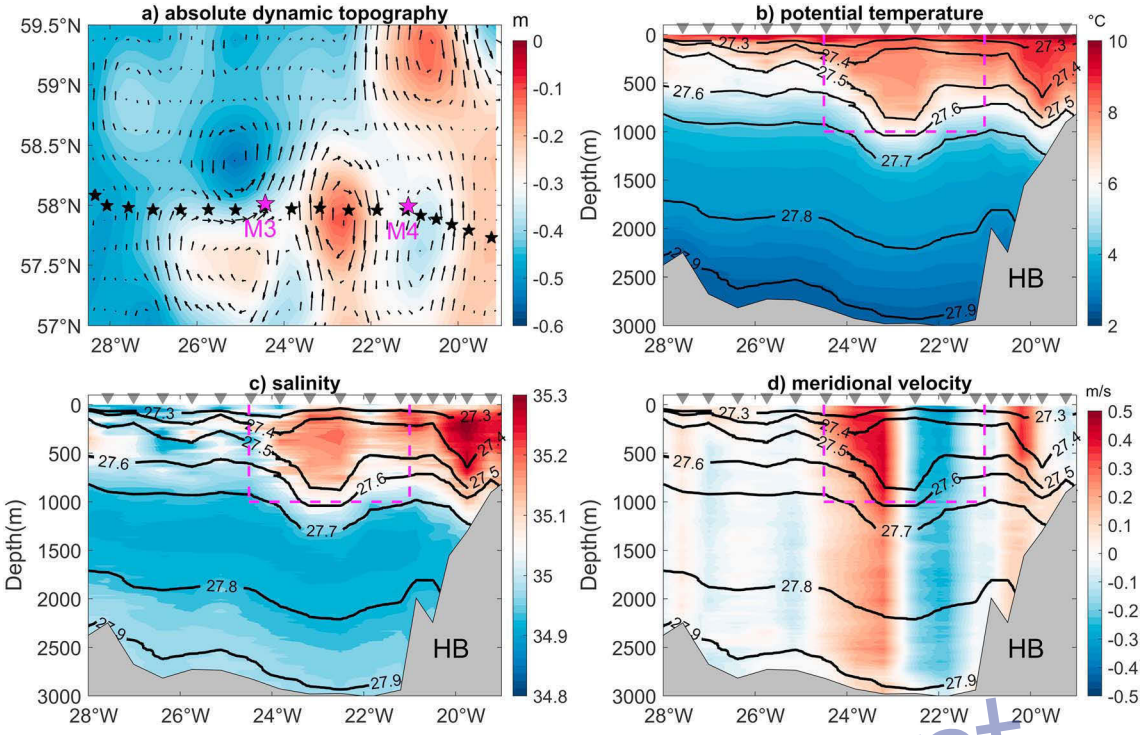

Figure 6. (a) The ADT map and the corresponding surface geostrophic velocity during a cruise in June 2015. The black pentagrams denote the CTD stations. The (b) potential temperature, (c) salinity, and (d) meridional velocity over the entire water column are shown. Velocity profiles are measured by the Lowered-ADCP. The gray triangles near the surface mark the locations for each profile. The magenta boxes denote the area surveyed by gliders.

pdfelement

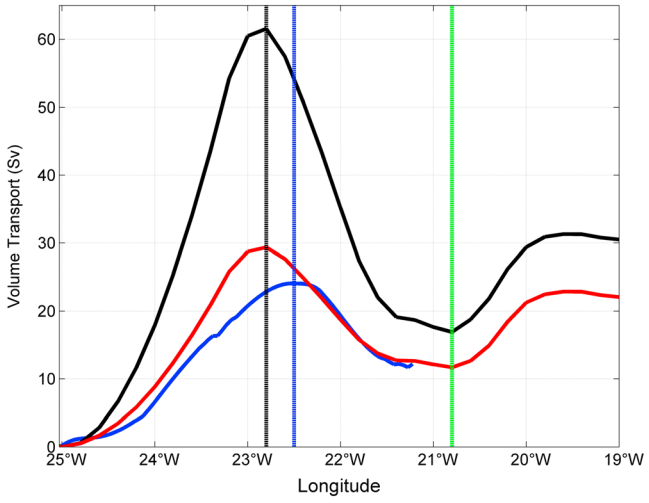

Figure 7. The Zonally Cumulative Volume Transport (ZCVT) is calculated from the observed meridional velocity collected by both glider and Lowered-ADCP. The starting point is 25°W where the northward velocity is nearly zero. The results in the full water column (black) and in the top 1,000 m (blue for glider and red for Lowered-ADCP). The dashed black and blue lines denote the locations for the maximum northward transport occur in Lowered-ADCP and glider data, respectively. The dashed green line illustrates the local minimum northward transport, which also marks the eddy eastern boundary. Unit: Sv.

and 6d). The weak southward flow west of 25°W is induced by the cyclonic eddy centered at 58.5°N (Figure 6a). There is a well-defined northward current over the western slope of the Hatton Bank, which is another NAC branch. The velocity over the slope is intensified in the top 500 m with maximum of about 0.3 m/s. The northward current is weaker below 500 m but still reaches about 0.1 m/s.

The eddy velocities between 25°W and 21°W indicate an asymmetric structure. The maximum northward velocity is about 0.45 m/s, while the maximum southward current is only about 0.37 m/s. The glider data yield similar result with the maximum northward of 0.39 m/s and the maximum southward of 0.32 m/s. The larger amplitude of northward velocity suggests that parts of the NAC impose onto the eddy velocity field.

To obtain further insight for the velocity structure in the Iceland Basin, we calculated the Zonally Cumulative Volume Transport (ZCVT) using the Lowered-ADCP data (Figure 7). The starting point is 25°W where the northward velocity is nearly zero. The northward transport across the eddy's western half is 61.5 Sv over the entire water column. The ZCVT is reduced east of 22.8°W due to the southward velocity in the eddy's eastern half. This leads to a local minimum of 16.9 Sv between 25°W and 20.8°W. While we do not know whether the pure eddy-related volume transport is zero, the net northward volume transport across the eddy definitely includes the NAC branch in the central Iceland Basin. Including another NAC branch over the slope, the ZCVT is further increased east of 20.8°W and reaches about 31.3 Sv at 19.6°W. Further eastward, the ZCVT remains almost constant until 19.0°W. We take

Remove Watermark Now

31.3 Sv as the upper limit for the possible NAC transport from the central Iceland Basin to the Hatton Bank during the observational period.

The ZCVT is also computed using both glider and the Lowered-ADCP observations in the top 1,000 m. The ZCVT in the top 1,000 m shows similar shape with the results over the entire water column. The maximum ZCVT value occurs near 22.8°W for the Lowered-ADCP data and 22.5°W for the glider observations. The slight shift in longitude is mostly due to the fact that the glider was advected when zonally cutting across the eddy. In the top 1,000 m, the maximum northward volume transport is 29.4 Sv in the Lowered-ADCP data and is larger than the 24.1 Sv estimated from the glider data. However, the results from both methods start to agree with each other east of 22.4°W. The overall agreement between these two estimates demonstrates that the glider data provide reliable measurement for the velocity structure. The total northward transport across the section is 22.1 Sv in the top 1,000 m, suggesting that the NAC distributes about two thirds of its volume transport in the upper ocean.

3.3. Dynamic Parameters for the Eddy

This section tries to estimate the dynamic parameters for the A1 eddy using observations. Given that the CTD section and the glider section almost cross the eddy center, the observed southward velocity in the eddy's eastern half can be regarded as its azimuthal velocity. It is used to represent the eddy's typical velocity, which is on the order of 0.3 m/s. The Rossby number $R_0 = U/fL$ is estimated to be about 0.04, where L refers to eddy's radius of 60 km. The small R_0 reveals that the eddy is dominated by the geostrophic dynamics. In addition, R_0 also reflects the ratio of relative vorticity (ζ) to planetary vorticity (f). This is helpful to interpret the potential vorticity (PV) estimated from observations.

The Ertel PV

$$Q_{\text{Ertel}} = \frac{\omega_a \cdot \nabla \rho_\theta}{\rho_0} = -\frac{(2\Omega + \nabla \times \vec{u}) \cdot \nabla \rho_\theta}{\rho_0} \tag{1}$$

where ω_a is the absolute vorticity, Ω denotes Earth's angular velocity, $\vec{u}$ is the three-dimensional velocity vector, ρ_θ is the potential density, and ρ_0 is the reference density.

Neglecting the vertical velocity, equation (1) can be further reorganized as

$$Q_{\text{Ertel}} = \frac{(f+\zeta)N^2}{g} + \frac{1}{\rho_0}\left(\frac{\partial v}{\partial z}\frac{\partial \rho_\theta}{\partial x} - \frac{\partial u}{\partial z}\frac{\partial \rho_\theta}{\partial y}\right) \tag{2}$$

where f is the Coriolis parameter, g is gravitational acceleration, and $\zeta = \frac{\partial v}{\partial x} - \frac{\partial u}{\partial y}$ is the vertical component of the relative vorticity. The squared buoyancy frequency $N^2 = -\frac{g}{\rho_0}\frac{\partial \rho_\theta}{\partial z}$.

To estimate Q_{Ertel} from observations, we consider the following two factors. The relative vorticity (ζ) is approximated by $\frac{\partial v}{\partial x}$. The meridional velocity (v) is either from Lowered-ADCP data or estimated using the depth-averaged current from glider data and the thermal wind relationship. While the dominant current in the Iceland Basin is northward, $\frac{\partial u}{\partial y}$ might no longer be negligible when an eddy is established. According to high-resolution numerical results, neglecting $\frac{\partial u}{\partial y}$ near the eddy would cause uncertainty for ζ as much as 20%–30%. As mentioned above, the ratio of ζ to f for the overall eddy domain is a small quantity, so that the uncertainties in ζ are not expected to have significant impact for our estimation.

The gliders were designed to repeatedly navigate along a zonal transect, so that they were mainly orientated along the intense zonal density gradient. While their pathways were detoured by ocean current, the observed $\frac{\partial \rho_\theta}{\partial x}$ (i.e., the zonal density gradient) is on the order of 10^{-5} kg/m^4 and is overwhelmingly larger than the meridional gradient $\left(\frac{\partial \rho_\theta}{\partial y}\right)$ whose magnitude is about10^{-7} kg/m^4. According to thermal wind relationship, $\frac{\partial u}{\partial z}$ is proportional to the meridional density gradient. As a result, $\frac{\partial u}{\partial z}\frac{\partial \rho_\theta}{\partial y} \ll \frac{\partial v}{\partial z}\frac{\partial \rho_\theta}{\partial x}$.

After incorporating the above two factors, equation (2) can be further simplified as

$$Q_{\text{Ertel|obs}} = \frac{\left(f + \frac{\partial v}{\partial x}\right)N^2}{g} + \frac{1}{\rho_0}\frac{\partial v}{\partial z}\frac{\partial \rho_\theta}{\partial x} \tag{3}$$

pdfelement

Remove Watermark Now

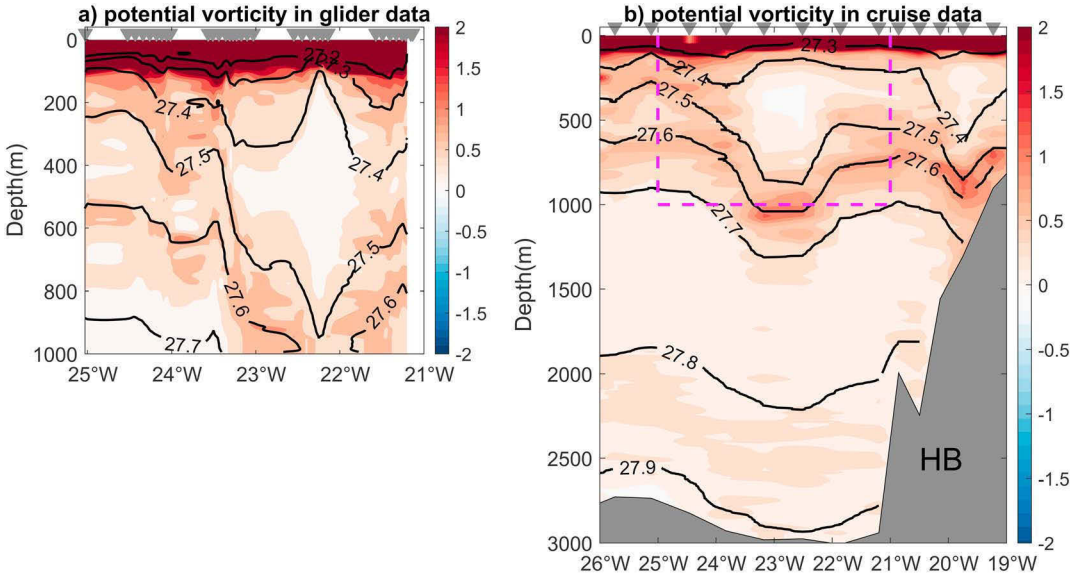

Figure 8. The Ertel potential vorticity estimated using (a) glider and (b) cruise data are shown in color. Unit: $10^{-9}\cdot m^{-1}\cdot s^{-1}$. The black lines denote the potential density (σ_θ). The gray triangles denote the locations for the glider profiles and CTD stations. The magenta dashed box in (b) marks the region surveyed by the gliders.

The first term denotes the stretching vorticity, and the second reflects the product of horizontal component of vorticity and buoyancy gradient.

According to equation (3), $Q_{Ertel}|_{obs}$ is estimated from observed hydrographic and meridional velocity (Figure 8). Overall, the relative vorticity is less than 5% of the stretching term, so that the Ertel PV profiles are dominated by the stretching vorticity. The highest $Q_{Ertel}|_{obs}$ is located near the surface, mainly above the isopycnal $\sigma_\theta = 27.3$. Another region with elevated PV is near the σ_θ level of 27.6, which is near the permanent pycnocline. The water properties in the eddy core are quite homogeneous, so that their $Q_{Ertel}|_{obs}$values are much smaller than the ambient waters. In addition, the region enclosed by σ_θ levels of 27.7 and 27.8 also shows relatively low PV. This depth range corresponds to the core waters in the LSW whose stratification is weak. Below σ_θ = 27.8, the stratification is increased near the interface between the LSW and ISOW. Consequently, $Q_{Ertel}|_{obs}$ in this region is higher than the LSW core waters in the above. The cruise data reveal that the NAC branch on the slope (about 20°W) also carries relatively low PV. In the following, we will show that the subsurface low PV is a typical signature in the eastern subpolar North Atlantic.

3.4. Eddy Origination

This section tries to compare the physical characteristics with the surrounding large-scale water masses with an aim to identify the eddy origination. The cruise data collected in July 2015 were confined within the Iceland Basin and were not sufficient to illustrate the large-scale structure for the hydrography and PV in the eastern subpolar region. Instead, another summer cruise performed in June 2014 along the OSNAP East line was analyzed with assumption that the large-scale water masses in 2014 and 2015 did not have significant changes. The overall patterns for the temperature and salinity along this section are characterized by a large-scale front with intense horizontal gradient in the Iceland Basin (Figure 9). Satellite ADT map shows that the CTD stations were located in the tail of an anticyclonic eddy whose center is about 59°N. Although only four stations were collected near the eddy, the depression of isopycnals between $\sigma_\theta = 27.4$ and $\sigma_\theta = 27.7$ is evident. The low PV waters between $\sigma_\theta = 27.3$ and $\sigma_\theta = 27.4$ extend eastward from central Iceland Basin to the Rockall Trough (Figure 9d). The highest PV occurs near the seasonal pycnocline and reaches a magnitude of about 2.0×10^{-9} $m^{-1}s^{-1}$. Another high PV region is the permanent pycnocline with typical value of about 1.0×10^{-9} $m^{-1}s^{-1}$. The low PV between permanent pycnocline and the base of seasonal pycnocline characterizes the typical SPMW (Brambilla et al., 2008; Johnson, 2007; McCartney & Talley, 1982; Tsuchiya et al., 1992). The PV within the SPMW is set in winter and is conserved in other seasons. Therefore, the low PV waters in the eddy core in year 2015 might originate from SPMW.

pdfelement

Remove Watermark Now

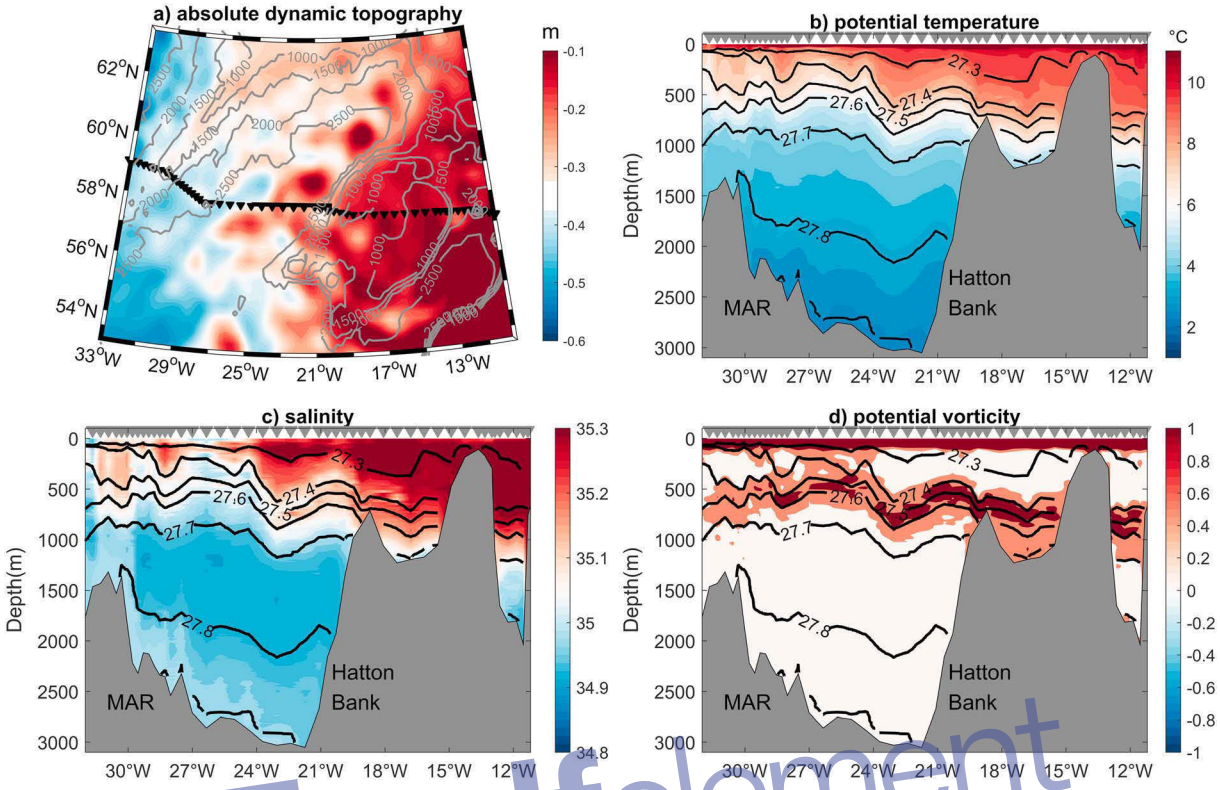

Figure 9. (a) The ADT map during a trans-basin cruise in June 2014 along the OSNAP East. The black triangles denote the CTD stations. The (b) potential temperature (unit: °C) and salinity collected by the cruise are shown, respectively. (d) The stretching vorticity ($\frac{fN^2}{g}$) estimated from the cruise data and its unit is $10^{-9} \cdot m^{-1} \cdot s^{-1}$.

pdfelement

Analysis of water properties on the temperature-salinity (T-S) diagram provides more insights on the eddy core waters. The SAIW and SPMW are the two major water masses for the upper ocean in the Iceland Basin. Their properties on the T-S curve are clearly distinct (Figure 10). The cold and fresh SAIW characterized by minimum salinity of 34.9 is located to the west of A1 eddy in 2015. The warm and salty SPMW lies on the east of the anticyclonic eddy. The typical densities for the eddy core waters are $\sigma_\theta = 27.3$ and $\sigma_\theta = 27.4$, and their T/S characteristics are apparently very close to the SPMW (Figure 10).

Additional information can be inferred from the satellite ADT maps, which illustrate the life cycle of the A1 eddy observed in July 2015. From late May 2015 closed contours in the ADT map started to emerge in a region between 23°W and 21°W near 58°N (Figure 11a). We take this as the initial stage of the A1 eddy. There was well-defined zonal ADT gradient in the central Iceland Basin, corresponding to a branch of northward current that flowed in parallel to the Hatton Bank. One month later, the A1 eddy moved westward to the central Iceland Basin and its center can be easily identified by elevated high ADT (Figure 11b). This is also the period when the cruise and glider data were collected. The eddy movement was tracked by visual examination of daily satellite ADT maps. The A1 eddy was found to stay in the central Iceland Basin for a few months. By early November 2015, the A1 eddy moved northward, probably advected by the northward flowing NAC (Figure 11c). It did not move further northward, but rather stayed around 58°N–59°N. The A1 eddy was apparently dissipated in early March 2016 (Figure 11d).

Based on the above analysis, we conclude that the anticyclonic eddy observed in 2015 was locally generated, near the western slope of the Hatton Bank. Part of the SPMW was trapped in the upper part of the eddy, so that its core waters have homogeneous properties and low PV. The eddy also has a strong barotropic component and it can be easily detected in satellite ADT maps.

4. Eddy Formation in Model Results

To further elucidate how the eddy in the Iceland Basin is formed, we analyzed numerical results from a high-resolution numerical simulation. We are not expecting that the model simulation exactly captures the

Remove Watermark Now

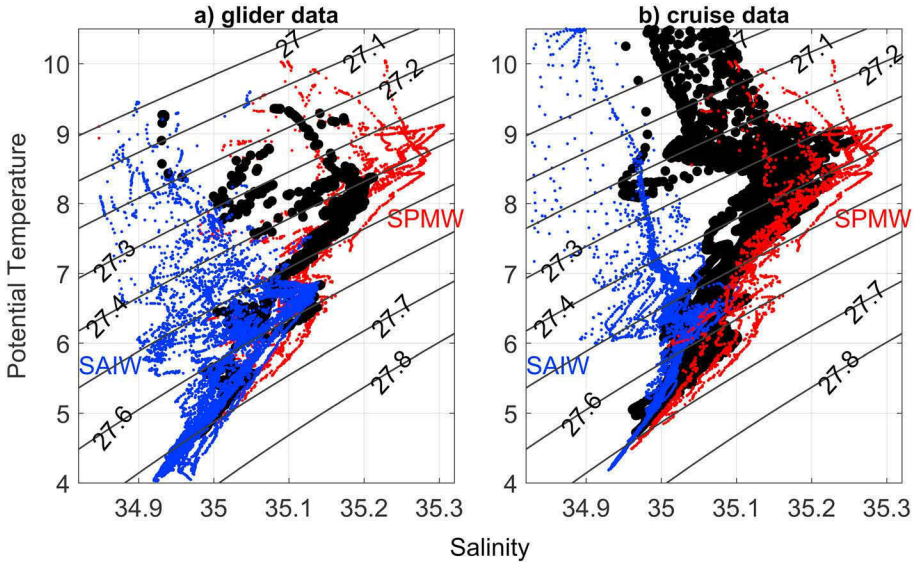

Figure 10. Potential temperature-salinity plot for the upper 1,000 m collected along 58°N in June 2015 for (a) glider data and (b) cruise data. The blue dots are profiles west of the eddy, showing the cold and fresh SAIW. The black dots are inside the eddy. The red dots denote profiles east of the eddy, featured by the warm and salty SPMW.

pdfelement

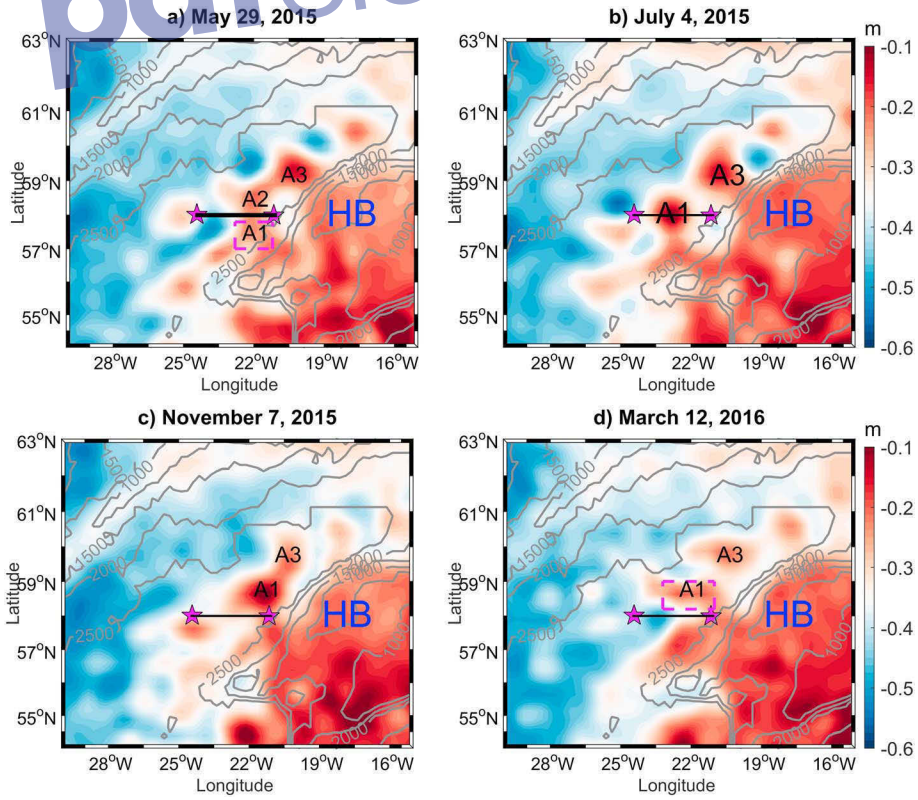

Figure 11. Satellite ADT in (a) 29 May 2015, (b) 4 July 2015, (c) 7 November 2015, and (d) 12 March 2016. The gray lines denote the isobaths at 2,500, 2,000, 1,500, and 1,000 m. The anticyclonic eddy investigated here is marked by "A1." The (a) very early and (d) late stages of the eddy are marked by magenta box. HB denotes the Hatton Bank.

Remove Watermark Now

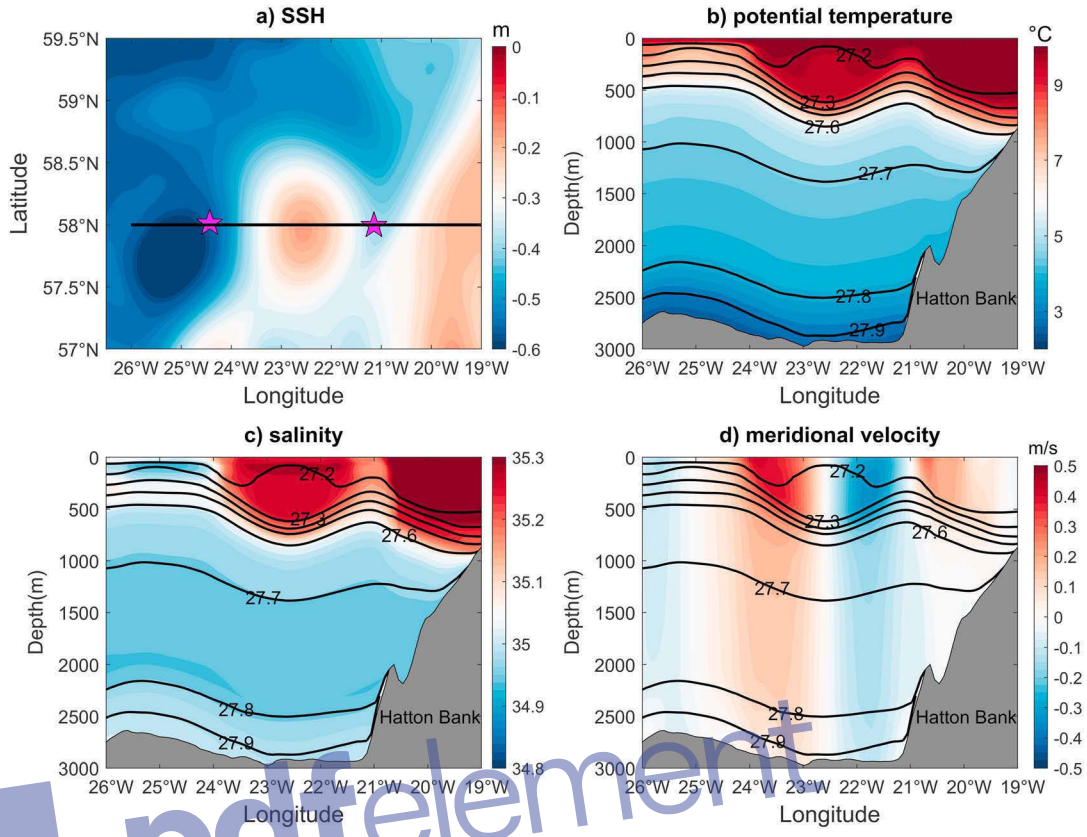

Figure 12. (a) The sea surface height (unit: m) in June 2005 showing an anticyclonic eddy along 58°N in the numerical model output. The magenta pentagrams reflect the endpoints of glider transect. The black line defines the section showing the (b) simulated potential temperature, (c) salinity, and (d) meridional velocity, respectively.

observed eddy in the right time and right place. Instead, we identified the anticyclonic eddy events whose initial formation times are late May, which is the same season for the observed anticyclonic eddy. Eddies in the numerical results were detected following the methodology of Nencioli et al. (2010). Figure 12 illustrates the composited sea surface height and the corresponding subsurface structure for the anticyclonic eddy events. The upper part carries homogeneous warm and salty waters, which are enclosed by σ_θ = 27.2 and σ_θ = 27.5. Below σ_θ = 27.6 is the LSW and ISOW. The northward velocity in the eddy's western side is stronger than its southward flowing counterpart in the east, indicating that one NAC branch is superimposed onto the eddy. The evident barotropic component in the eddy velocity reveals its deep reaching influence. Another NAC branch carrying the warm and salty SPMW is located on the western slope of the Hatton Bank. West of the eddy is the colder and fresher SAIW. Thus, the overall characteristics for the simulated eddy and the surrounding velocity structure are quite similar to the one in observations. We note that the permanent pycnocline near σ_θ = 27.6 is shallower in the model than in the observations, perhaps due to the model's insufficient diapycnal mixing between different water masses. However, this does not change our following analysis about the eddy formation.

Examination of the sea surface height in the model outputs suggests that the anticyclonic eddies usually first show up near the steep topographic slope on the western flanks of the Hatton Bank. To understand how the eddy is formed, we analyzed the Ertel PV structure prior to the eddy formation. Similar to the observations, the Ertel PV is dominated by the stretching term and highlights the seasonal and permanent pycnoclines as high PV regions (Figure 13a). Within the quasi-geostrophic framework, the PV gradient changing sign is the necessary condition for the classic baroclinic and barotropic instability (Pedlosky, 1987). We therefore calculate the zonal and vertical gradient of PV with an aim to diagnose the conditions for instabilities. The zonal PV gradient has elevated negative and positive values between σ_θ = 27.2 and σ_θ = 27.6, which is the permanent thermocline (Figure 13b). Similarly, the vertical PV gradient change signs near the base of seasonal and

Remove Watermark Now

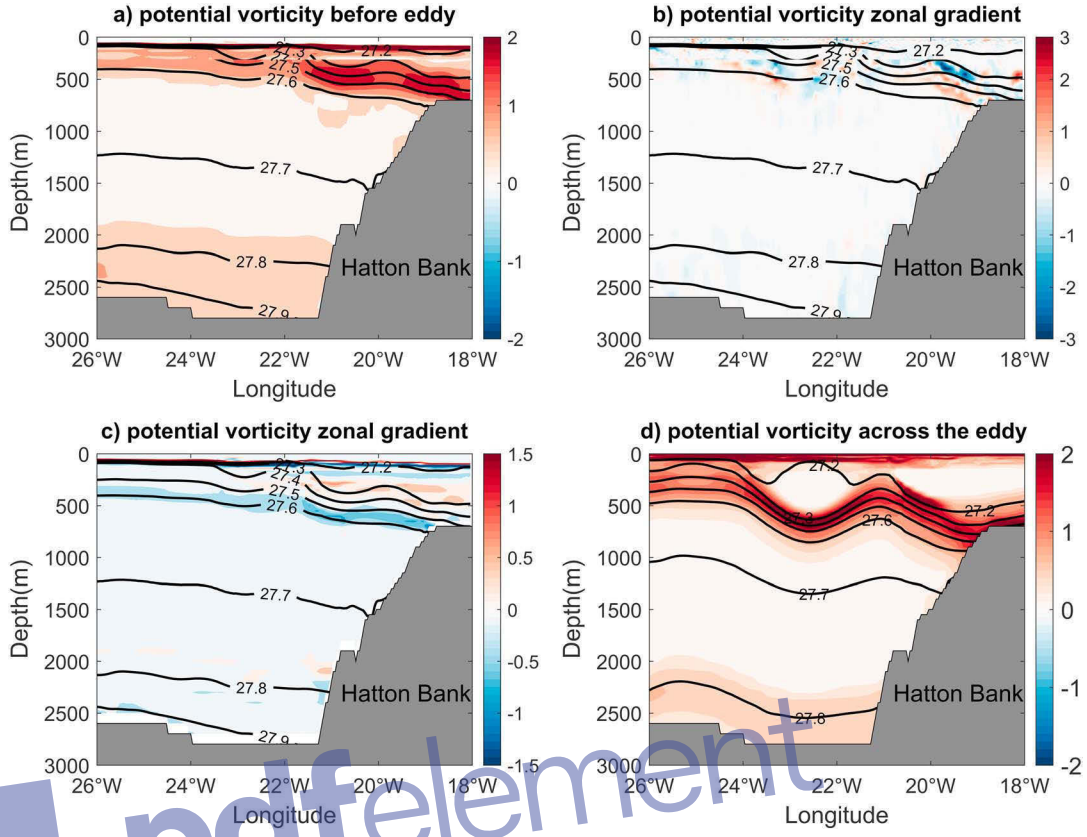

Figure 13. (a) The Ertel PV calculated from the model results during the periods when the anticyclonic eddies have not appeared. Unit:$10^{-9} \cdot m^{-1} \cdot s^{-1}$. (b and c) The zonal and vertical gradient of Ertel PV. Unit:$10^{-13} \cdot m^{-2} \cdot s^{-1}$. (d) The Ertel PV corresponding to the stable stage of the eddy is shown. Unit:$10^{-9} \cdot m^{-1} \cdot s^{-1}$.

pdfelement

permanent thermoclines. The sign changes for the PV gradient are particularly evident over the slope region. Therefore, the structure for the PV gradient meets the necessary conditions for instabilities. Once established, the eddy has a similar PV structure to the observations, where low PV waters are trapped in the eddy center (Figure 13b). Another low PV region in the upper ocean lies on top of the Hatton Bank where the SPMW is also found. This further demonstrates that the eddy core waters in the upper ocean share similar properties with the SPMW, which is in line with the findings inferred from observations.

To further elucidate the specific process for eddy growth, we calculate the energy transformation in the numerical results. The energy transfer from mean background potential energy to eddy is through the baroclinic instability. While this energy conversion can be quantified by vertical advection of density, our numerical simulation did not directly output the vertical velocity. Here we use both horizontal advection of density anomaly and the isopycnal slope of the basic state to estimate the energy transfer induced by baroclinic instability. This method was adopted by Spall et al. (2008) to analyze the energy conversion terms for the western arctic shelfbreak eddies in both mooring data and numerical results. In the Iceland Basin, the SAF maintains a strong isopycnal slope in the zonal direction and the meridional isopycnal slope for the background state is negligible. Therefore, the energy conversion is given by

$$E_{BC} = -g\alpha\overline{u'\rho_\theta'}/\rho_0$$

where α is the mean isopycnal slope, the primes denote anomalies with respect to the time average, and u is the zonal velocity. The isopycnal slope is computed by $\frac{\partial Z_\rho}{\partial x}$ where Z_ρ is the depth of isopycnal and x is zonal distance. Eleven-year model outputs between 2005 and 2015 are used to calculate the time mean and the corresponding prime terms. We first show the eddy density flux $\overline{u'\rho_\theta'}$, which is the most important term in E_{BC}. The positive eddy density flux represents the eastward transport of density anomaly by the eddy. The

Remove Watermark Now

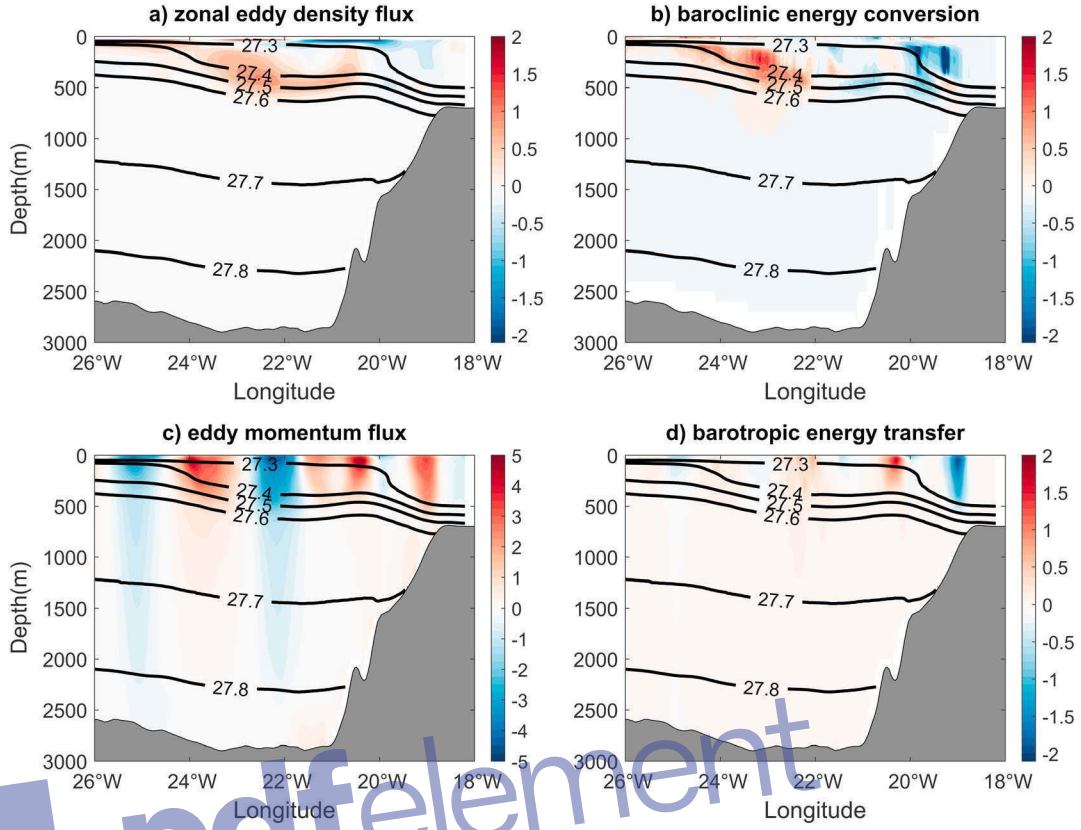

Figure 14. (a) Eddy density flux (10^{-2} kg · m^{-2} · s^{-1}), (b) baroclinic energy conversion term (10^{-8} m^2/s^3), (c) eddy momentum flux (10^{-3} m^2/s^2), and (d) barotropic energy transfer term (10^{-8} m^2/s^3). Please refer to texts on their calculation. The black lines denote the potential density (σ_θ).

pdfelement

positive eddy density flux mainly occurs near the permanent pycnocline with highest value around the steep isopycnal slope (Figure 14a). The zonal eddy density flux acts to flatten the permanent pycnocline, which is to release potential energy from the SAF.

The baroclinic energy conversion (E_{BC}) is determined by both eddy density flux and the mean isopycnal slope. The positive value in E_{BC} denotes that energy is converted from the mean potential energy into eddy. As illustrated in Figure 14b, the elevated positive values in E_{BC} are concentrated near the largest isopycnal slope, which is determined by the eddy density flux. This region is the central Iceland Basin where the eddy is fully established. The negative E_{BC} over the slope region coincides with the NAC branch here, implying that this branch of background flow is enhanced when the eddy emerges. Note that the isopycnals near 22°W have opposite tilt with those near the SAF, so the E_{BC} in this region is negative and energy is not converted to eddy.

The energy transfer from mean kinetic energy to the eddy energy is related to barotropic instability (Spall et al., 2008). The NAC branches in the Iceland Basin are parts of the large-scale circulation so that they contain substantial kinetic energy. The energy conversion associated with barotropic instability is given by

$$E_{BT} = \overline{u'v'}V_x$$

where u and v are the zonal and meridional velocity at each snapshot and the primes denote anomalies with respect to the time average. V is the time-averaged meridional flow. The kinetic energy transfer is computed from 11-year model outputs (2005–2015). We first discuss the eddy momentum flux $\overline{u'v'}$, which is the most important term in E_{BT}. The eddy momentum flux represents the eddy's impact on the meridional velocity field. There are alternating positive and negative values along the zonal direction in the eddy momentum flux field (Figure 14c). The positive values indicate that meridional momentum is carried

Remove Watermark Now

eastward and negative ones reveal westward momentum transport. Apparently, the alternating structure in the eddy momentum flux leads to horizontal convergence and divergence in the eddy meridional momentum. The convergence would pile up the eddy meridional momentum, which is to produce northward eddy velocity. Correspondingly, the horizontal divergence of the eddy momentum flux would generate southward eddy velocity. The strongest convergence and divergence take place near the zero crossings in the eddy momentum flux, which are about the same locations for the northward and southward flows associated with the eddy (Figure 12d). In addition, the eddy momentum flux vertically extends from surface to ocean bottom, which agrees with the barotropic structure in the eddy velocity profiles.

The energy transfer from the mean kinetic energy to eddy energy (E_{BT}) is a product of eddy momentum flux and the zonal shear of the mean background flow. Positive values in E_{BT} represent the energy converted into eddy. Most positive values in E_{BT} occur above the permanent pycnocline, which has weaker stratification and stronger horizontal shear in the mean background northward flow. This indicates that the northward flowing NAC can trigger barotropic instability in the upper ocean and contribute to the eddy's development. This pattern agrees with the theoretical results in Poulin et al. (2014), who pointed out that the signature of barotropic instability prevails in the upper water column for a surface-intensified current. It is worth noting that negative E_{BT} can be seen near top of the Hatton Bank. Although a similar behavior is also found in the baroclinic energy conversion (E_{BC}), their locations are different. The barotropic conversion occurs near the flat isopycnal region, but the baroclinic term mainly takes place near the isopycnal slope. Both terms suggest that the NAC branch in this region can be accelerated during the eddy event. This is consistent with the obvious northward velocity on the slope found in both observations and model results.

5. Summary and Discussion

pdfelement

The high EKE in the Iceland Basin has been known for a long time (Chafik et al., 2014; Heywood et al., 1994; Lankhorst & Zenk, 2006). An anticyclonic eddy observed with an autonomous glider and ship-based hydrographic observations in summer 2015 is presented here. The eddy size is quite large with a diameter of 120 km. According to Shoosmith et al. (2005), this scale is typical for the anticyclonic eddies in the Iceland Basin. The waters in the eddy core have a lens-like structure with warm and salty properties. The strong barotropic currents reflect the eddy's bottom reaching influence. These features are in concert with several anticyclonic eddies previously found in the Iceland Basin (e.g., Martin et al., 1998; Wade & Heywood, 2001).

Another distinctness of the anticyclonic eddies in the Iceland Basin is their longevity. The eddy studied here was sustained for about 10 months. Other anticyclonic eddies were found to survive for more than six to seven months and even one year (Martin et al., 1998; Read & Pollard, 2001). Some floats were found to be enclosed in an eddy for about 14 months (Shoosmith et al., 2005). This long life cycle might have significant impacts on the regional circulation, especially on the time scale longer than seasonal.

The homogeneous waters in the eddy core originated from the SPMW on the slope, and they pushed the shallow isopycnals toward the surface. The isopycnal $\sigma_\theta = 27.4$ was the upper boundary for the eddy core waters, and it was domed up to about 100 m near the eddy center. This makes it much easier to be affected by the seasonal air-sea interactions. Once ventilated by strong surface cooling, the weakly stratified core waters will be easily modified. This means that the upper 1,000 m within the eddy is susceptible to the strong air-sea flux changes. The observed eddy was established in May 2015 and maintained a coherent structure until March 2016. Similar long-lived eddies were frequently found in the satellite data in this region (e.g., Read & Pollard, 2001). It is therefore reasonable to speculate that some eddies would encounter strong winter cooling and its properties might be modified by the winter convection.

Moreover, the eddy carried warm and salty SPMW and spent the majority of its life cycle in the central Iceland Basin where the SAF was located. Through lateral stirring and horizontal heat and salt fluxes, the eddy is expected to facilitate the water exchange across the SAF. For instance, the cold and fresher SAIW can gain heat and salt input when the eddy is collapsed. To obtain a quantitative estimation about eddy's impact, the eddy radius is taken as 60 km and the local water depth is about 3,000 m. Assuming that the eddy is a symmetric ring, the volume within the eddy is of 3.39×10^{13} m^3. The examinations of satellite ADT maps suggest that about two eddies per year are generated near the glider section. Thus, the eddy can lead to an annualized northward transport of 2.1 Sv.

Remove Watermark Now

In earlier studies, eddies in the Iceland Basin were also found to provide favorable conditions to enhance the rate of primary production (e.g., Savidge & Williams, 2001; Woodward & Rees, 2001). The doming of upper ocean isopycnals in the eddy center can enhance the near surface stratification, which is crucial for the ecosystem in the subpolar ocean. In fact, the North Atlantic Bloom Experiment demonstrated that the eddy-driven stratification and subduction in the Iceland Basin contribute to the initiation of the North Atlantic spring phytoplankton bloom and export of organic carbon into the deeper ocean (Mahadevan et al., 2012; Omand et al., 2015).

Anticyclonic eddies carrying warm and salty core waters have also frequently been found in the Labrador Sea, Irminger Sea, and the Lofoten Basin. Fan et al. (2013) summarized the characteristics of the observed anticyclones in these regions. The specific ranges for their temperature and salinity properties were closely linked to the source regions and their formation seasons, so that their core water properties exhibited large variations. Even though different criteria were adopted to determine the eddy sizes, their diameters were generally less than 60 km. This is much less than the 120 km found in this study. It should be mentioned that the baroclinic Rossby deformation radius in the Iceland Basin is about 10–15 km. The larger eddy size in the Iceland Basin is likely due to the barotropic instability associated with the NAC (J. H. LaCasce, personal communication, May 2018). More importantly, all the observed anticyclones, including the one in the Iceland Basin, have low Rossby numbers. This clearly shows that the overall dynamics in these anticyclonic eddies are dominated by geostrophy.

The anticyclonic eddies simulated by high-resolution model simulations were used to explore the eddy formation. The zonal and vertical PV gradient prior to the eddy event exhibits negative and positive values near the seasonal and permanent pycnoclines. Consequently, they satisfy the necessary conditions for barotropic and baroclinic instabilities. The unstable structure is more evident over the western slope of the Hatton Bank. This is in line with satellite maps, which suggest that the eddy first appears near the slope region and later on moves westward to the central Iceland Basin. The eddy does not move further westward, perhaps because the isobaths change from 3,000 m in the central Iceland Basin to about 2,500 m at 28°W (Figure 6). In addition, the eddy fluxes and energy conversion terms in the model indicate that the eddy is fed by the mean potential energy at the isopycnal slope associated with the SAF and by the mean kinetic energy in the upper ocean.

Eddies generated by currents over topographic slopes had been widely studied (LaCasce, 1998; Spall, 2004; Stewart & Thompson, 2015; Poulin et al., 2014; Wang & Stewart, 2018). The basin-scale circulation flowing in parallel with topography is a general feature in the subpolar North Atlantic. The large-scale current intensifies over steep topography slope and can trigger the barotropic and baroclinic instabilities. This process is believed to be responsible for the IR formation in the eastern boundary of the Labrador Sea (Bracco et al., 2008; Bracco & Pedlosky, 2003; Katsman et al., 2004; Luo et al., 2011; Prater, 2002; Spall, 2004). Similar mechanisms are also found in the Lofoten Basin where eddies are shed by the Norwegian Atlantic Current flowing along the Norwegian coast (Isachsen, 2015; Kohl, 2007). The eddy formation analyzed here is in line with the above studies and expands our understanding about eddy generation in the subpolar North Atlantic.

Acknowledgments
The glider field work was funded by the Cooperative Research Initiative between the Woods Hole Oceanographic Institution (WHOI) and the Ocean University of China. The authors wish to acknowledge B. Hodges, H. Furey at WHOI, and the captains and crews of the research vessels *Pelagia* and *Discovery* for their assistance in the deployment, recovery, and operations of the gliders. The CTD, LADCP, and ADCP data used in this study were collected by the OSNAP project and generously provided by W. Johns and A. Papapostolou from University of Miami. The support from U. S. NSF for A. B. (OCE-1258823) and J. Z. and J. Y. (OCE-1634886) are appreciated. X. L. was supported by China's National Key Research and Development Projects (2016YFA0601803) and the Fundamental Research Funds for the Central Universities (201424001 and 201362048). We thank Mike Spall for the helpful comments and suggestions. Comments and suggestions from anonymous reviewers are very helpful to improve the manuscript. The hydrographic data from the World Ocean Database 2013 (WOD 2013) were downloaded at https://www.nodc.noaa.gov/OC5/WOD13/. The satellite altimeter products are distributed by the Copernicus Marine and Environment Monitoring Service (http://www.marine.copernicus.eu). The cruise data are available at the CLIVAR and Carbon Hydrographic Data Office (http://cchdo.ucsd.edu/) under section name AR07E. The glider data can be obtained through https://dx.doi.org/10.7924/r4m905g03.

References

Arhan, M. (1990). The North Atlantic Current and Subarctic Intermediate Water. *Journal of Marine Research*, *48*(1), 109–144. https://doi.org/10.1357/002224090784984605

Bersch, M. (2002). North Atlantic Oscillation-induced changes of the upper-layer circulation in the northern North Atlantic Ocean. *Journal of Geophysical Research*, *107*(C10), 3156. https://doi.org/10.1029/2001JC000901

Bower, A. S., & von Appen, W.-J. (2008). Interannual variability in the pathways of the North Atlantic Current over the Mid-Atlantic Ridge and impact of topography. *Journal of Physical Oceanography*, *38*, 104–120. https://doi.org/10.1175/2007JPO3686.1

Bracco, A., & Pedlosky, J. (2003). Vortex generation by topography in locally unstable baroclinic flows. *Journal of Physical Oceanography*, *33*(1), 207–219. https://doi.org/10.1175/1520-0485(2003)033%3C0207:VGBTIL%3E2.0.CO;2

Bracco, A., Pedlosky, J., & Pickart, R. S. (2008). Eddy formation near the west coast of Greenland. *Journal of Physical Oceanography*, *38*(9), 1992–2002. https://doi.org/10.1175/2008JPO3669.1

Brambilla, E., & Talley, L. D. (2008). Subpolar Mode Water in the northeastern Atlantic: 1. Averaged properties and mean circulation. *Journal of Geophysical Research*, *113*, C04025. https://doi.org/10.1029/2006JC004062

Brambilla, E., Talley, L. D., & Robbins, P. E. (2008). Subpolar Mode Water in the northeastern Atlantic: 2. Origin and transformation. *Journal of Geophysical Research*, *113*, C04026. https://doi.org/10.1029/2006jc004063

Brandt, P., Schott, F. A., Funk, A., & Martins, C. S. (2004). Seasonal to interannual variability of the eddy field in the Labrador Sea from satellite altimetry. *Journal of Geophysical Research*, *109*, C02028. https://doi.org/10.1029/2002JC001551

Chafik, L., Rossby, T., & Schrum, C. (2014). On the spatial structure and temporal variability of poleward transport between Scotland and Greenland. *Journal of Geophysical Research, Oceans*, *119*, 824–841. https://doi.org/10.1002/2013JC009287

pdfelement

Remove Watermark Now

Daniault, N., Mercier, H., Lherminier, P., Sarafanov, A., Falina, A., Zunino, P., et al. (2016). The northern North Atlantic Ocean mean circulation in the early 21st century. *Progress in Oceanography*, *146*, 142–158. https://doi.org/10.1016/j.pocean.2016.06.007

De Jong, M. F. (2010). Hydrographic variability in the Irminger Sea, PhD Thesis, Utrecht University, Utrecht, the Netherlands, pp. 208.

De Jong, M. F., Bower, A. S., & Furey, H. H. (2016). Seasonal and inter-annual variations of Irminger Ring formation and boundary-interior heat exchange in FLAME. *Journal of Physical Oceanography*, *46*(6), 1717–1734. https://doi.org/10.1175/JPO-D-15-0124.1

De Jong, M. F., van Aken, H. M., Våge, K., & Pickart, R. S. (2012). Convective mixing in the central Irminger Sea: 2002–2010. *Deep-Sea Research Part I*, *63*, 36–51. https://doi.org/10.1016/j.dsr.2012.01.003

DeJong, M. F., Bower, A. S., & Furey, H. H. (2014). Two years of observations of warm core anticyclones in the Labrador Sea and their seasonal cycle in heat and salt stratification. *Journal of Physical Oceanography*, *44*(2), 427–444. https://doi.org/10.1175/jpo-d-13-070.1

Eden, C., & Böning, C. (2002). Sources of eddy kinetic energy in the Labrador Sea. *Journal of Physical Oceanography*, *32*(12), 3346–3363. https://doi.org/10.1175/1520-0485(2002)032%3C3346:SOEKEI%3E2.0.CO;2

Fan, X., Send, U., Testor, P., Karstensen, J., & Lherminier, P. (2013). Observations of Irminger Sea anticyclonic eddies. *Journal of Physical Oceanography*, *43*(4), 805–823. https://doi.org/10.1175/JPO-D-11-0155.1

Fratantoni, D. M. (2001). North Atlantic surface circulation during 1990's observed with satellite-tracked drifters. *Journal of Geophysical Research*, *106*(C10), 22,067–22,093. https://doi.org/10.1029/2000JC000730

García-Ibáñez, M. I., Pardo, P. C., Carracedo, L. I., Mercier, H., Lherminier, P., Ríos, A. F., & Pérez, F. F. (2015). Structure, transports and transformations of the water masses in the Atlantic Subpolar Gyre. *Progress in Oceanography*, *135*, 18–36. https://doi.org/10.1016/j.pocean.2015.03.009

Han, G., & Ikeda, M. (1996). Basin-scale variability in the Labrador Sea from TOPEX/POSEIDON and Geosat altimeter data. *Journal of Geophysical Research*, *101*(C12), 28,325–28,334. https://doi.org/10.1029/96JC02778

Harris, R. P., Boyd, P., Harbour, D. S., Head, R. N., Pingree, R. D., & Pomroy, A. J. (1997). Physical, chemical and biological features of a cyclonic eddy in the region of 61° 10′N, 10° 50′W in the North Atlantic. *Deep Sea Research, Part I*, *44*, 1815–1839.

Hátún, H., Eriksen, C. C., & Rhines, P. B. (2007). Buoyant eddies entering the Labrador Sea observed with gliders and altimetry. *Journal of Physical Oceanography*, *37*(12), 2838–2854. https://doi.org/10.1175/2007JPO3567.1

Heywood, K. J., McDonagh, E. L., & White, M. (1994). Eddy kinetic energy of the North Atlantic subpolar gyre from satellite altimetry. *Journal of Geophysical Research*, *99*, 22,525–22,539.

Holliday, N., Bacon, S., Allen, J., & McDonagh, E. (2009). Circulation and transport in the western boundary currents at cape farewell, Greenland. *Journal of Physical Oceanography*, *39*(8), 1854–1870. https://doi.org/10.1175/2009JPO4160.1

Houpert, L., Inall, M., Dumont, E., Gary, S., Johnson, C., Porter, M., et al. (2018). Structure and Transport of the North Atlantic Current in the Eastern Subpolar Gyre from Sustained Glider Observations. *Journal of Geophysical Research: Oceans*, *123*. https://doi.org/10.1029/2018JC014162

Isachsen, P. E. (2015). Baroclinic instability and the mesoscale eddy field around the Lofoten basin. *Journal of Geophysical Research: Oceans*, *120*, 2884–2903. https://doi.org/10.1002/2014JC010448

Jakobsen, P. K., Ribergaard, M. H., Quadfasel, D., Schmith, T., & Hughes, C. W. (2003). Near-surface circulation in the northern North Atlantic as inferred from Lagrangian drifters: Variability from the mesoscale to interannual. *Journal of Geophysical Research*, *108*(C8), 3251. https://doi.org/10.1029/2002JC001554

Johnson, G. C. N. (2007). Gruber, decadal water mass variations along 20°W in the northeastern Atlantic Ocean. *Progress in Oceanography*, *73*(3-4), 277–295. https://doi.org/10.1016/j.pocean.2006.03.022

Katsman, C., Spall, M., & Pickart, R. (2004). Boundary current eddies and their role in the restratification of the Labrador Sea. *Journal of Physical Oceanography*, *34*(9), 1967–1983. https://doi.org/10.1175/1520-0485(2004)034%3C1967:BCEATR%3E2.0.CO;2

Kohl, A. (2007). Generation and stability of a quasi-permanent vortex in the Lofoten Basin. *Journal of Physical Oceanography*, *37*(11), 2637–2651. https://doi.org/10.1175/2007JPO3694.1

LaCasce, J. H. (1998). A geostrophic vortex over a slope. *Journal of Physical Oceanography*, *28*(12), 2362–2381. https://doi.org/10.1175/1520-0485(1998)028%3C2362:AGVOAS%3E2.0.CO;2

Lankhorst, M., & Zenk, W. (2006). Lagrangian observations of the middepth and deep velocity fields of the northeastern Atlantic Ocean. *Journal of Physical Oceanography*, *36*(1), 43–63. https://doi.org/10.1175/JPO2869.1

Lherminier, P., Mercier, H., Huck, T., Gourcuff, C., Perez, F. F., Morin, P., et al. (2010). The Atlantic meridional overturning circulation and the subpolar gyre observed at the A25-OVIDE section in June 2002 and 2004. *Deep Sea Research, Part I*, *57*(11), 1374–1391. https://doi.org/10.1016/j.dsr.2010.07.009.

Lilly, J. M., & Rhines, P. B. (2002). Coherent eddies in the Labrador Sea observed from a mooring. *Journal of Physical Oceanography*, *32*(2), 585–598. https://doi.org/10.1175/1520-0485(2002)032%3C0585:CEITLS%3E2.0.CO;2

Lilly, J. M., Rhines, P. B., Schott, R., Lavender, K., Lazier, J., Send, U., & D'Asaro, E. (2003). Observations of the Labrador Sea eddy field. *Progress in Oceanography*, *59*(1), 75–176. https://doi.org/10.1016/j.pocean.2003.08.013

Lozier, M. S., et al. (2017). Overturning in the Subpolar North Atlantic Program: A new international ocean observing system. *Bulletin of the American Meteorological Society*, *98*(4), 737–752. https://doi.org/10.1175/BAMS-D-16-0057.1

Luo, H., Bracco, A., & Di Lorenzo, E. (2011). The interannual variability of the surface eddy kinetic energy in the Labrador Sea. *Progress in Oceanography*, *91*(3), 295–311. https://doi.org/10.1015/j.pocean.2011.01.006

Mahadevan, A., D'Asaro, E., Perry, M.-J., & Lee, C. (2012). Eddy-driven stratification initiates North Atlantic spring phytoplankton blooms. *Science*, *337*(6090), 54–58. https://doi.org/10.1126/science.1218740

Martin, A. P., Wade, I. P., Richards, K. J., & Heywood, K. J. (1998). The PRIME eddy. *Journal of Marine Research*, *56*(2), 439–462. https://doi.org/10.1357/002224098321822375

McCartney, M. S., & Talley, L. D. (1982). The Subpolar Mode Water of the North Atlantic Ocean. *Journal of Physical Oceanography*, *12*, 1169–1188. https://doi.org/10.1175/1520-0485(1982)012%3C1169:TSMWOT%3E2.0.CO;2

Nencioli, F., Dong, C., Dickey, T., Washburn, L., & McWilliams, J. C. (2010). A vector geometry based eddy detection algorithm and its application to a high-resolution numerical model product and high-frequency radar surface velocities in the Southern California bight. *JAOT*, *27*(3), 564–579. https://doi.org/10.1175/2009JTECHO725.1

Omand, M. M., D'Asaro, E. A., Lee, C. M., Perry, M.-J., Briggs, N., Cetinic, I., & Mahadevan, A. (2015). Eddy-driven subduction exports particulate carbon from the spring bloom. *Science*, *348*(222), 54–58. https://doi.org/10.1126/science.1260062

Pacariz, S., Hátún, H., Jacobsen, J. A., Johnson, C., Eliasen, S. K., & Rey, F. (2016). Nutrient-driven poleward expansion of the Northeast Atlantic mackerel (Scomber scombrus) stock: A new hypothesis. *Elementa: Science Anthropocene*, *4*, 105. https://doi.org/10.12952/journal.elementa.000105

Pedlosky, J. (1987). *Geophysical fluid dynamics*. New York: Springer. 1987. xiv −/− 710pp

pdfelement

Remove Watermark Now

Pollard, R. T., Griffiths, M. J., Cunningham, S. A., Read, J. F., Pérez, F. F., & Ríos, A. F. (1996). Vivaldi 1991: A study of the formation, circulation and ventilation of Eastern North Atlantic Central Water. *Progress in Oceanography*, *37*(2), 167–192. https://doi.org/10.1016/S0079-6611(96)00008-0

Pollard, R. T., Read, J. F., & Holliday, N. P. (2004). Water masses and circulation pathways thorugh the Iceland Basin during Vivaldi 1996. *Journal of Geophysical Research*, *109*, C04004. https://doi.org/10.1029/2003JC002067

Poulin, F., Stegner, A., Hernandez-Arencibia, M., Marrero-Diaz, A., & Sangra, P. (2014). Steep shelf stabilization of the Bransfield Coastal Current: Linear stability analysis. *Journal of Physical Oceanography*, *44*, 714–732. https://doi.org/10.1175/JPO-D-13-0158.1

Prater, M. (2002). Eddies in the Labrador Sea as observed by profiling RAFOS floats and remote sensing. *Journal of Physical Oceanography*, *32*(2), 411–427. https://doi.org/10.1175/1520-0485(2002)032%3C0411:EITLSA%3E2.0.CO;2

Read, J. F., & Pollard, R. T. (2001). A long-lived eddy in the Iceland Basin 1998. *Journal of Geophysical Research*, *106*(C6), 11,411–11,421. https://doi.org/10.1029/2000JC000492

Reverdin, G., Niiler, P. P., & Valdimarsson, H. (2003). North Atlantic Ocean surface currents. *Journal of Geophysical Research*, *108*(C1), 3002–3004.

Rhein, M., Kieke, D., Huettl-Kabus, S., Roessler, A., Mertens, C., Meissner, R., et al. (2011). Deep water formation, the subpolar gyre, and the meridional overturning circulation in the subpolar North Atlantic. *Deep Sea Research Part II: Topical Studies in Oceanography*, *58*(17-18), 1819–1832. https://doi.org/10.1016/j.dsr2.2010.10.061

Roessler, A., Rhein, M., Kieke, D., & Mertens, C. (2015). Long-term observations of North Atlantic Current transport at the gateway between western and eastern Atlantic. *Journal of Geophysical Research: Oceans*, *120*, 4003–4027. https://doi.org/10.1002/2014JC010662

Rykova, T., Straneo, F., Lilly, J. M., & Yashayaev, I. (2009). Irminger Current anticyclones in the Labrador Sea observed in the hydrographic record, 1990–2004. *Journal of Marine Research*, *67*(3), 361–384. https://doi.org/10.1357/002224009789954739

Sarafanov, A., Falina, A., Mercier, H., Sokov, A., Lherminier, P., Gourcuff, C., et al. (2012). Mean full-depth summer circulation and transports at the northern periphery of the Atlantic Ocean in the 2000s. *Journal of Geophysical Research*, *117*, C01014. https://doi.org/10.1029/2011JC007572

Savidge, G., & Williams, P. J. L. B. (2001). The PRIME 1996 cruise: An overview. *Deep Sea Research, Part II*, *48*(4-5), 687–704. https://doi.org/10.1016/S0967-0645(00)00111-9

Shoosmith, D. R., Richardson, P. L., Bower, A. S., & Rossby, H. T. (2005). Discrete eddies in the northern North Atlantic as observed by looping RAFOS floats. *Deep Sea Research, Part II*, *52*(3-4), 627–650. https://doi.org/10.1016/j.dsr2.2004.12.011

Spall, M. A. (2004). Boundary currents and water mass transformation in marginal seas. *Journal of Physical Oceanography*, *34*(5), 1197–1213. https://doi.org/10.1175/1520-0485(2004)034%3C1197:BCAWTI%3E2.0.CO;2

Spall, M. A., Pickart, R. S., Fratantoni, P. S., & Plueddemann, A. J. (2008). Western Arctic shelfbreak eddies: Formation and transport. *Journal of Physical Oceanography*, *38*(8), 1644–1668. https://doi.org/10.1175/2007JPO3829.1

Stewart, A. L., & Thompson, A. F. (2015). Eddy-mediated transport of warm Circumpolar Deep Water across the Antarctic shelf break. *Geophysical Research Letters*, *42*, 432–440. https://doi.org/10.1002/2014GL062281

Stoll, M. H. C., van Aken, H. M., de Baar, H. J. W., & Kraak, M. (1996). Carbon dioxide characteristics of water masses in the northern North Atlantic. *Marine Chemistry*, *55*(1996), 217–232.

Thurnherr, A. M. (2011). How to process LADCP data with the LDEO software. [Available online at ftp://ftp.ldeo.columbia.edu/pub/LADCP/HOWTO].

Tsuchiya, M., Talley, L. D., & McCartney, M. S. (1992). An eastern Atlantic section from Iceland southward across the equator. *Deep Sea Research*, *39*(11-12), 1885–1917. https://doi.org/10.1016/0198-0149(92)90004-D

Våge, K., & Coauthors (2011). The Irminger Gyre: Circulation, convection, and interannual variability. *Deep Sea Research*, *I*(58), 590–614.

Van Aken, H. M. (1995). Mean currents and current variability in the Iceland Basin. *Netherlands Journal of Sea Research*, *33*(2), 135–145. https://doi.org/10.1016/0077-7579(95)90001-2

Van Aken, H. M., & Becker, G. (1996). Hydrography and through-flow in the northeastern North Atlantic Ocean: The NANSEN project. *Progress in Oceanography*, *38*(4), 297–346. https://doi.org/10.1016/S0079-6611(97)00005-0

Vellinga, M., & Woods, R. A. (2002). Global impacts of a collapse of the Atlantic thermohaline circulation. *Climatic Change*, *54*(3), 251–267. https://doi.org/10.1023/A:1016168827653

Volkov, D. L. (2005). Interannual variability of the altimetry-derived eddy field and surface circulation in the extratropical North Atlantic Ocean in 1993–2001. *Journal of Physical Oceanography*, *35*(4), 405–426. https://doi.org/10.1175/JPO2683.1

Wade, I. P., & Heywood, K. J. (2001). Tracking the PRIME eddy using satellite altimetry. *Deep Sea Research, Part II*, *48*(4-5), 725–737. https://doi.org/10.1016/S0967-0645(00)00094-1

Wang, Y., & Stewart, A. (2018). Eddy dynamics over continental slopes under retrograde winds: Insights from a model inter-comparison. *Ocean Modelling*, *121*, 1–18. https://doi.org/10.1016/j.ocemod.2017.11.006

White, M. A., & Heywood, K. J. (1995). Seasonal and interannual changes in the North Atlantic subpolar gyre from Geosat and TOPEX/Poseidon altimetry. *Journal of Geophysical Research*, *100*(C12), 24,931–24,941. https://doi.org/10.1029/95JC02123

Wolfe, C., & Cenedese, C. (2006). Laboratory experiments on eddy generation by a buoyant coastal current flowing over variable topography. *Journal of Physical Oceanography*, *36*(3), 395–411. https://doi.org/10.1175/JPO2857.1

Woodward, E. M. S., & Rees, A. P. (2001). Nutrient distributions in an anticyclonic eddy in the northeast Atlantic Ocean, with reference to nanomolar ammonium concentrations. *Deep Sea Research, Part II*, *48*(4-5), 775–793. https://doi.org/10.1016/S0967-0645(00)00097-7

Xu, X., Hurlburt, H. E., Schmitz, W. J. Jr., Fischer, J., Zantopp, R., & Hogan, P. J. (2013). On the currents and transports connected with the Atlantic meridional overturning circulation in the subpolar North Atlantic. *Journal of Geophysical Research: Oceans*, *118*, 502–516. https://doi.org/10.1002/jgrc. 20065

Xu, X., Schmitz, W. J. Jr., Hurlburt, H. E., & Hogan, P. J. (2012). Mean Atlantic meridional overturning circulation across 26.5°N from eddy-resolving simulations compared to observations. *Journal of Geophysical Research*, *117*, C03042. https://doi.org/10.1029/2011JC007586

Xu, X., Schmitz, W. J. Jr., Hurlburt, H. E., Hogan, P. J., & Chassignet, E. P. (2010). Transport of Nordic Seas overflow water into and within the Irminger Sea: An eddy-resolving simulation and observations. *Journal of Geophysical Research*, *115*, C12048. https://doi.org/10.1029/2010JC006351

Yashayaev, I. (2007). Hydrographic changes in the Labrador Sea, 1960–2005. *Progress in Oceanography*, *73*(3–4), 242–276. https://doi.org/10.1016/j.pocean.2007.04.015

Zhang, R. (2015). Mechanisms for low-frequency variability of summer Arctic sea ice extent. *Proceedings of the National Academy of Sciences of the United States of America*, *112*(15), 4570–4575. https://doi.org/10.1073/pnas.1422296112

Zhao, J., Bower, A., Yang, J., Lin, X., & Holliday, N. P. (2018). Meridional heat transport variability induced by mesoscale processes in the subpolar North Atlantic. *Nature Communications*, *9*(1), 1124. https://doi.org/10.1038/s41467-018-03134-x

pdfelement